M. Sertoli et al.

Modication of Impurity Transport in the Presence of Saturated (m, n)=(1,1) MHD Activity at ASDEX Upgrade

Modification of impurity transport in the presence of saturated (m,n)=(1,1) MHD activity at ASDEX Upgrade

M Sertoli, R. Dux, T. Pütterich and the ASDEX Upgrade Team

Max-Planck-Institut für Plasmaphysik, Boltzmannstraße 2, D-85748 Garching, Germany

E-mail: `marco.sertoli@ipp.mpg.de`

Abstract. Impurity transport analysis based on argon impurity injection in sawtoothing plasmas in the presence of long lived inter-crash $(m, n) = (1, 1)$ MHD activity is analysed in an ASDEX Upgrade discharge. In order to describe the time-evolution of the SXR time-traces after the impurity injection two sets of transport coefficients are necessary, switching at the onset of the $(1, 1)$ mode. The non-linear time evolution of the background SXR emissivity which has to be subtracted in order to perform the transport analysis leads to systematic errors that cannot be eliminated from the analysis. In such conditions, typical experimental methods for the determination of the transport coefficients are demonstrated to be inapplicable and ideas for new ways to probe impurity transport in the presence of long-lived MHD activity are given. These can be then applied to study e.g. the mitigation of central impurity accumulation by ECRH which is most of the times accompanied by strong saturated $(1, 1)$ modes.

1. Introduction

Most experimental impurity transport studies in tokamak plasmas are of perturbative nature and rely on a few very important assumptions:

1. the injected impurity is a "trace", not effecting the quasi-neutrality condition nor the power balance;

2. the background plasma parameters and geometry are constant in the time-range of analysis;

3. the impurity transport parameters are constant in the time-range of analysis;

4. the transport of different ionization stages of the impurity is governed by the same set of transport parameters;

5. the impurity density is constant on a flux surface.

If the injected impurity is in trace approximation and it doesn't affect the background plasma (condition *1*), its transport will be governed by the background plasma parameters only. If these parameters are constant (condition *2*) then the transport characteristics of the impurity will also be constant (condition *3*).

Because of the Z-dependence of both neoclassical and turbulent transport (see e.g. [1] and [2]), condition *4* is generally not satisfied. It's effect can be neglected for fully stripped impurities, for analysis which measure one ionization stage only, e.g. charge exchange recombination spectroscopy (CXRS) (see e.g. [3]) or in those cases where the analysis is limited to charge states close to one another ($\Delta q/Z << 1$, where q is the charge state of the ion of atomic number Z). In all other cases, the results will be an *effective* set of transport coefficients averaged over the different ionization stages.

The constance of the impurity density on a flux surface (condition *5*) has recently been relaxed from a theoretical point of view since a few codes can now account for poloidal asymmetries due to centrifugal effects and poloidally varying electrostatic potential which can effect the transport [4, 5, 6, 7]. The results from the codes have been used to model the impurity photon emission in the soft X-ray spectral region and compared to the experimental profiles as detected by the soft X-ray (SXR) diagnostic [8, 9].

For a typical analysis, the radial flux of the impurity ions after their injection is modelled in one dimension (radial) assuming poloidal symmetry and one set of transport coefficients for all ionization stages. The modelled ionization balance and relative emission characteristics (known from atomic data calculations) are then used to evaluate the radiated power so to match the time evolution of experimental spectroscopic signals (see e.g. [10, 11, 12, 13, 14, 15, 16]). Other methods require the experimental determination of the total impurity density profile and its time evolution after the injection. In this case, the transport coefficients are evaluated as the slope and offset (corresponding to diffusion and convection respectively) of the linear fit of the normalized impurity particle flux on the normalized impurity density [17]. In general, whatever method or diagnostic is used for the determination of the transport coefficients, if any of the conditions above are not met, impurity injection experiments will not yield physically relevant results but only an *effective* set of transport coefficients.

This is what happens in the presence of long-lived, large amplitude $(m, n) = (1, 1)$ internal kink magneto-hydro-dynamic (MHD) instabilities. Due to the non-axisymmetric equilibrium arising in the presence of the rigid displacement of the plasma core within the $q = 1$ surface, the plasma geometry is not retrievable from typical equilibrium reconstructions. Since this non-axisymmetric equilibria is furthermore varying on transport time-scales, condition *2* isn't valid anymore. Assuming that the retrieved transport parameters are representative of an *effective* mode-averaged transport, variations in the experimental signals which must be linked to changes in transport have been observed, thus violating condition *3* as well. Despite having been qualitatively described in more than one publication in the past decades (see e.g. [18, 19, 20, 21]) only one attempt to quantify these changes in transport have been made for JET plasmas [21].

This contribution aims to provide such a quantification for an example argon impurity injection in an ASDEX Upgrade (AUG) discharge and to demonstrate the general limited- or non-applicability of classical experimental methods for the study of impurity transport in the presence of saturated/long-lived $(m, n) = (1, 1)$ mode

activity and of MHD instabilities in general. The method described in [17] for the evaluation of the transport coefficients is reviewed in section 2. The analysed experiment is described in section 3 and the results of the transport analysis are discussed in section 4. An alternative analysis method is proposed in section 5, applicable to machines with high enough intrinsic W concentration so that the SXR signals are dominated by its emission, as is the case for AUG or the Joint European Torus (JET). Discussion on the implications of the results and conclusions are given in section 6.

2. Method for the determination of the impurity transport coefficients

The transport parameters have been evaluated following the method described in [17]. For clarity, the main points of the method are described again here.

The radial transport of an impurity A of atomic number Z is described through $Z + 1$ coupled differential equations [19]:

$$\frac{\partial n_{A,q}(r,t)}{\partial t} = -\frac{1}{r}\frac{\partial}{\partial r}[r\,\Gamma_{A,q}(r,t)] + Q_{A,q}(r,t) \tag{1}$$

where $\Gamma_{A,q}(r,t)$ is the ion particle flux, $n_{A,q}(r,t)$ the ion density and $Q_{A,q}(r,t)$ the external sources and sinks connecting the various ionization stages q. Choosing the radial coordinate $r = \sqrt{V/(2\pi^2 R_{axis})}$ where V is the volume within the flux surface and R_{axis} the major radius of the plasma axis and averaging all quantities over the flux surface, each equation can be written in cylindrical geometry while still accounting for non-circular plasma cross sections [19, 22].

Summing equations 1 over all the ionization stages, all source terms besides $Q_{A,1}$ (ionization of the neutral atom and recombination of the first ionization stage) drop out. Considering only the transport inside the separatrix where the neutral source usually vanishes, one obtains an equation for the total impurity ion density that can be inverted to evaluate the total ion flux:

$$\Gamma_A(r,t) = -\frac{1}{r}\int_0^r \frac{\partial n_A(r',t)}{\partial t}\,r'\,dr' \tag{2}$$

Assuming a diffusive and convective ansatz for this flux, the transport coefficients can be recovered from the slope (D) and offset (v) of the linear fit of the normalized flux on the normalized density gradient:

$$\frac{\Gamma_A(r,t)}{n_A(r,t)} = -\frac{D(r)}{n_A(r,t)}\frac{\partial n_A(r,t)}{\partial r} + v(r) \tag{3}$$

where D and v are assumed equal for all ionization stages and constant in time. Equation 3 is the so-called *Gradient-Flux* relation (from now on referred as *G-F*). In order to apply this equation to evaluate the impurity transport coefficients, the total impurity ion density of impurity A must be known. This can be estimated using the SXR diagnostic.

The local emissivity of impurity A detected by the SXR diodes can be modelled as:

$$\epsilon_A^{sxr}(r,t) = n_e(r,t)\,n_A(r,t)\,L_A^{sxr}(r,t) \tag{4}$$

where n_e is the electron density, n_A the total impurity density and L_A^{sxr} the radiation loss parameter (also called *cooling factor*) filtered according to the filter function of the diagnostic (photon energy $\sim 1 - 20\ keV$ for the SXR diagnostic at AUG). The

detected brightness is the integral of equation 4 along the different lines-of-sight (LoS) (see [23] for details on the SXR diagnostic installed on AUG).

The radiation loss parameter $L_A^{sxr} = \sum_q f_{A,q} \, k_{A,q}^{sxr}$ depends on the filtered photon emissivity rate coefficients ($k_{A,q}^{sxr}$) and on the distribution of the charge states ($f_{A,q}$). The former depends on the filter function and on electron temperature and density, the latter on the electron temperature as well as on the transport parameters. For the case of the typical plasma parameters accessible at AUG (pedestal top temperature $< 1 \, keV$), with the presently installed Be-filters the L_A^{sxr} is found to be relatively insensitive to variations in transport. If evaluated using a standard set of transport coefficients and the plasma parameters of the discharge under analysis it can be considered constant [17]. For this reason, performing an Abel inversion of the raw SXR LoSs to evaluate the local SXR emissivity and subtracting the background prior to impurity injection, the total impurity ion density can be calculated by simply rearranging equation 4:

$$n_A(r,t) = \frac{\epsilon_{exp}^{sxr}(r,t)}{n_e(r,t) \, L_A^{sxr}(r,t)} \tag{5}$$

where $\epsilon_{exp}^{sxr}(r,t)$ is the background subtracted, Abel-inverted experimental SXR emissivity profile.

For the impurities under consideration in this contribution (Ar and W) the main contributions to L_A^{sxr} come from spontaneous line-emission occurring from electron-impact excited states. This means that the $1 \, keV$ photon energy sensitivity limit of the SXR diagnostic corresponds approximately to electron temperatures of $1 \, keV$. Accounting for possible inaccuracies in the filter-function and for transport which may lead to a broadening of the emissivity shells, equation 5 will be applied only within the conservative detection limit of $T_e > 1.3 \, keV$. As will be explained in the next sections, if the absolute calibration of the diodes is not known but the different channels are correctly cross-calibrated, a rescaling factor can be obtained using passive spectroscopy measurements of the impurity density.

3. Description of the experiment

The example reported is that of an argon injection experiment in a nitrogen-seeded lower-single-null AUG H-mode discharge (# 25447, plasma geometry as in figure 1g). The main plasma parameters of this discharge were: plasma current $I_P = 1 \, MA$, magnetic field $B_t = -2.5 \, T$, external heating $P_{NBI} = 7.5 \, MW$ (neutral beam injection) and $P_{ECRH} = 0.8 \, MW$ (electron cyclotron resonance heating). The ECRH deposition position is located just inside the $q = 1$ surface, located at $\rho_{pol}(q = 1) \sim 0.31$ in normalized poloidal flux coordinates, corresponding to an average minor radius at mid-plane of $\langle r(q = 1) \rangle \sim 14cm$. From now on the normalized poloidal flux radius $\rho_{pol} = \sqrt{(\psi - \psi_a)/(\psi_s - \psi_a)}$ will be used, where ψ is the poloidal flux and the indices s and a refer to the seperatrix and magnetic axis respectively.

The effect of the Ar injection (blue trace in figure 1e) is clearly visible in the time traces of the SXR diagnostic (figure 1f). The N2-puff strength (red in figure 1e), feedback controlled on the divertor temperature obtained from online measurements of the thermoelectric currents flowing between the inner and outer divertor [24], decreases slightly accounting for the power radiated by the injected argon ($< 5 \, \%$ increase in the total radiated power, blue trace in figure 1c). The line averaged electron density (figure 1b) increases of $< 5 \, \%$ just after the Ar injection. The sawtooth period is

slightly modified for 2 cycles in the decay phase of the injected Ar, visible in the electron temperature time-traces from electron cyclotron emission diagnostic (ECE)
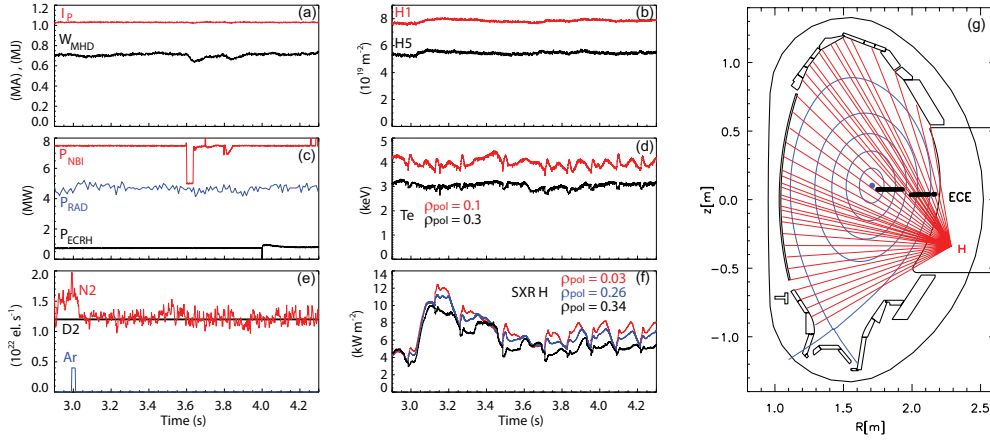

Figure 1. *Main plasma parameters of AUG discharge # 25447 in the time-range of interest (see text for full description) and the plasma cross-section (right) with the LoS of camera H of the SXR diagnostic and the measurement positions of the ECE diagnostic (black points)*
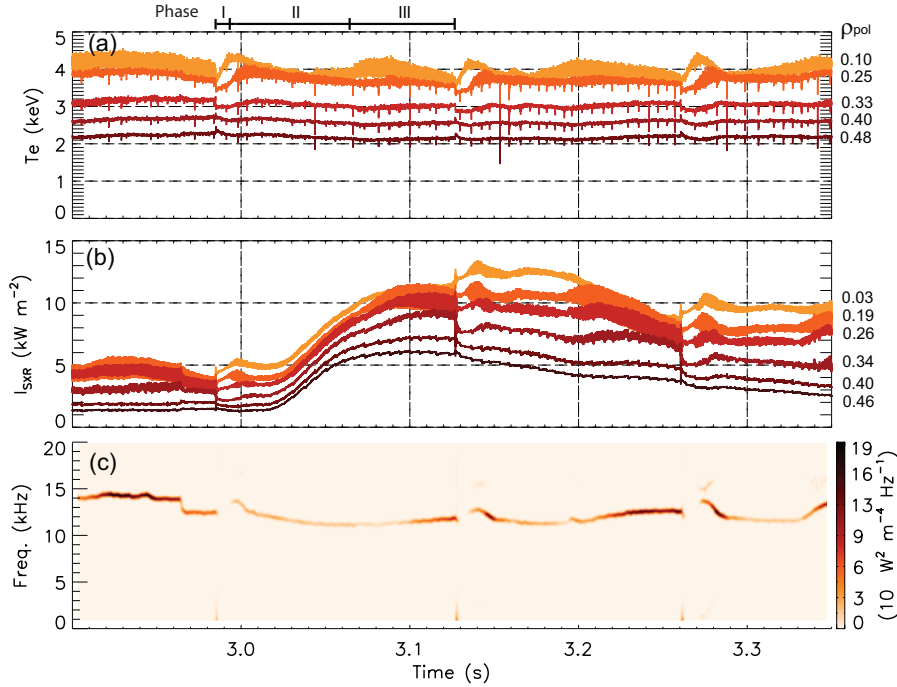

Figure 2. *Time evolution of (a) the electron temperature from ECE and (b) of the SXR LoSs around the time of impurity injection (3 seconds). The radial locations (in ρ_{pol}) of the ECE channels and impact parameters of the SXR LoSs are labelled on the right of the plots. (c) spectrogram of the most central SXR LoS.*

in figure 1d in time-range $3.25 - 3.7\ s$, returning afterwards to it's undisturbed pattern. No effects on the plasma energy are detectable (black in figure 1a) and the frequency of edge localized modes (ELMs) also remains constant throughout the time range of interest ($\sim 150\ Hz$, not shown in the plot)

A closer look at the ECE time traces close to the Ar-puff (figure 2a) shows that the electron temperature does not vary significantly within a sawtooth cycle, exhibiting excursions $< 5\%$ with respect to the sawtooth-averaged value. Three phases in the Te time-evolution can be clearly distinguished:

  I) *recovery phase* - steep rise just after the crash (lasting $< 10\%$ of the sawtooth period $\tau_{ST} \sim 140\ ms$);

 II) *quasi-stationary phase* - relatively constant electron temperature with weak mode activity ($\sim 50\%$ of τ_{ST});

III) *saturation phase* - mode growth and saturation ($\sim 40\%$ of τ_{ST}).

Providentially, the Ar-puff (at $3\ s$) occurs in the quasi-stationary phase (II) just after a sawtooth crash, the influx ending before the next crash takes place. This enables to probe one full sawtooth cycle (excluding the recovery phase) with the injected impurity.

3.1. Evolution of the background SXR signals

Since the application of equation 5 for the calculation of the impurity density requires the subtraction of the background prior to the Ar injection, a closer look at the
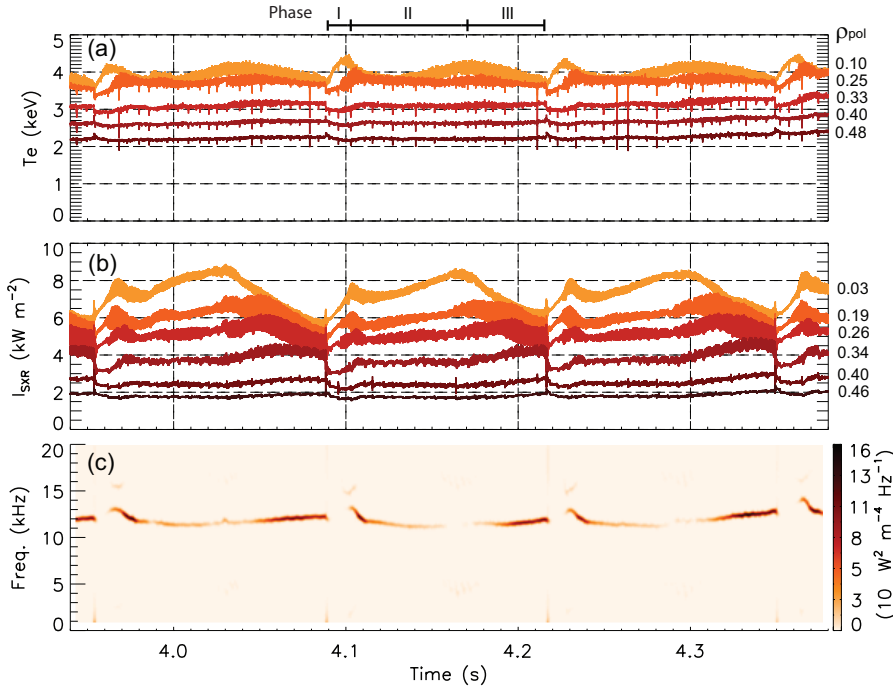

Figure 3. *Time evolution of: (a) the electron temperature from ECE and (b) the SXR LoSs one second after the impurity injection (same channels as in figure 2). (c) spectrogram of the most central SXR LoS.*

background sawtooth cycles is necessary before proceeding with the calculation of the transport coefficients. The impurity injection was performed quite close to a step-up in NBI heating power (at 2.6 s). Since no changes occur after the decay of the Ar signal and the recovery of the undisturbed sawtooth cycle (for $t > 3.7$ s), the background evolution at 4 s will be inspected.

The electron temperature in this phase of the discharge (figure 3a) follows the same three-phase cycle described previously. The background SXR LoS-integrals seem to qualitatively follow the electron temperature evolution in the first two phases, but behave rather differently during mode growth and saturation (figure 3b) where the brightness of the most central LoS-integrals decrease strongly. The crash is inverted with respect to typical sawteeth, the intensity of the most central LoSs increasing at the crash while the ones around and outside of the inversion radius $\rho_{pol} \sim 0.37$ decrease.

Throughout the whole time-range of interest $t = [3.0, 4.5]$ s (during both Ar-puff and background cycles examined) the intrinsic W concentration evaluated by passive vacuum-ultra-violet (VUV) spectroscopy [25] shows only slight variations inside the q=1 surface ($c_{W,l} \sim 3 - 4 \cdot 10^{-5}$) and at mid radius ($c_{W,qc} \sim 2 - 3 \cdot 10^{-5}$). Details of these spectroscopic measurements are given in section 5. At these radii and in the same time-range, the effective charge evaluated by integrated data analysis (IDA) [26] is constant in time and flat inside the $q = 1$ surface: $Z_{eff}(\rho_{pol} < \rho_{pol,q=1}) \sim 1.3$ and $Z_{eff}(\rho_{pol} = 0.7) \sim 1.7$. Using the Z_{eff} profile to evaluate the deuterium density from the quasi-neutrality condition and, assuming the tungsten concentration constant along the radius at an average value of $\langle c_W \rangle = 3 \cdot 10^{-5}$, the different contributions to the SXR emissivity (D, low-Z impurities contributing to Z_{eff}, W) can be evaluated. The SXR emission is found to be clearly dominated by tungsten for $\rho_{pol} < 0.4$, accounting for $\sim 70\%$ of the total emission.

Since no other medium- / high-Z element is present in AUG discharges in a large enough concentration to contribute substantially to the SXR emission and, since the Z_{eff} profile is constant in time, the time evolution of the background sawtooth cycles will be solely caused by variation in background plasma parameters and tungsten density. In order to decouple these effects, the LoS-integrated SXR brightness is simulated for W-only emission assuming the W density constant in time and using the experimentally varying electron temperature and density profiles. Any deviation of the simulated signals from the experimental values will thus reflect modifications in the T_e and n_e profiles only. By normalising each simulated LoS to its experimental value just after the sawtooth crash (at ~ 4.22 s), the assumed c_W profile will not affect the final result. The electron temperature and density profiles for the simulation are taken from IDA fits of ECE and Li-beam + DCN interferometer [27, 28]. The simulated signals are shown in blue in the plots in figures 4a-f and compared with the experimental LoSs (same colour code as in figure 3, impact parameter labelled on the right of each plot). The dashed blue segments are time intervals where the Li-beam did not measure (IDA fits not available) for which an interpolation of the available electron density and temperature time-points has been performed.

The comparison of the experimental and modelled SXR brightness shows that its time evolution is completely governed by the electron temperature and density profile evolution for the two channels furthest form the centre (figures 4e-f) indicating that no variation in c_W is taking place outside of $\rho_{pol} \geq 0.4$. More central channels (figures 4a-c) show instead completely different patterns. Following the three-phase cycle described previously: recovery phase (I) the increase in SXR brightness is much
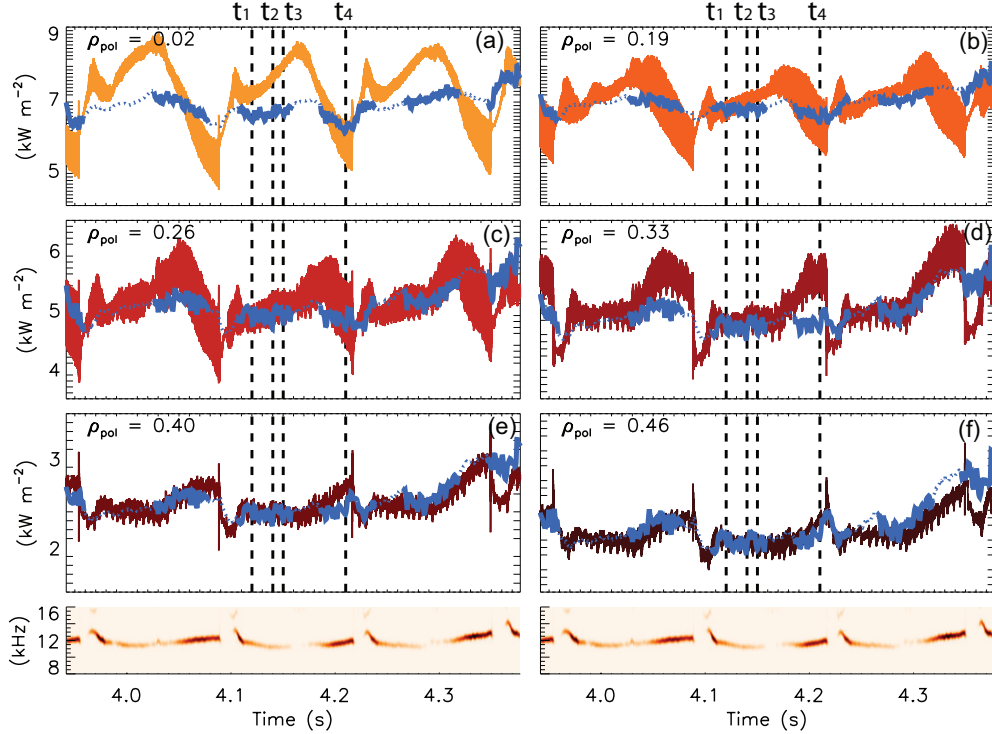
Figure 4. *Time evolution of the SXR LoSs shown in figure 3 compared with simulated signals (blue lines) normalized to the experimental values at the start of the last sawtooth cycle (~ 4.22 s). Bottom plots show the spectrogram of the most central SXR LoS for reference.*

stronger than what induced by variations of background plasma parameters; quasi-stationary phase (II) an initial decay is followed by a slow increase while T_e and n_e would keep the SXR brightness constant; saturation phase (III) during mode growth and saturation the most central SXR channels decrease drastically while the effects of T_e and n_e are still negligible. Because any deviation of the experimental time traces from the blue curves is caused by changes in the tungsten density and since the three phases show very different evolutions, each phase must be governed by a different set of transport parameters. The argon injection taking place in the quasi-stationary phase (II) where the variations in the electron profiles are negligible and its influx finishing at the end of the saturation phase (at the sawtooth crash), the transport of the argon should be described by two sets of transport coefficients. Finally, since the SXR brightness in the quasi-stationary phase (II) undergoes variations of $\sim 10\%$ with respect to the intensity increase caused by the Ar, the background in this phase can be assumed constant.

4. Evaluation of the transport coefficients

Using the methods described in [17] and briefly reviewed in section 2, the argon transport coefficients have been calculated for the quasi-stationary phase II (time range $3.015 - 3.075$ s in figure 2) and the saturation phase III (time range $3.075 -$

3.11 s). In order to minimize systematic errors due to possible different sensitivity curves of the various SXR cameras, the analysis has been performed using camera H only (LoS shown in figure 1g).

4.1. Phase II: weak mode activity

For the analysis of the quasi-stationary phase II $(3.015 - 3.075\ s)$, after having performed an Abel inversion of all available LoS of camera H, the background at $t_{bgnd} = 3.01\ s$ has been subtracted for the evaluation of the total argon density through equation 5. The transport coefficients have been then evaluated using the G-F relation within the sensitivity range of the SXR diagnostic ($\rho_{pol} \leq 0.6$), while for $\rho_{pol} > 0.6$ the convection and diffusion coefficients have been fixed to constant values so to match the observed evolution in SXR brightness of the outermost channels. The obtained diffusion and convection coefficient profiles within $\rho_{pol} \leq 0.6$ are shown in figure 5a and 5b (diamond symbols, labelled G-F), their ratio $v/D = \nabla n_A/n_A$ in figure 5c.

Since D and v are a result of the linear fit of the normalised impurity flux versus the normalised impurity density, their error bars reflect those on both the Abel inversion and the electron density used in equation 3. The large error bars inside $\rho_{pol} < 0.3$ are due to the fact that only a small amount of argon has reached the centre within the short time range of the analysis ($\sim 60\ ms$). In order to correct this and at the same time check the results obtained for larger radii, a sensitivity analysis scanning the transport coefficients has been performed: STRAHL [22] simulations
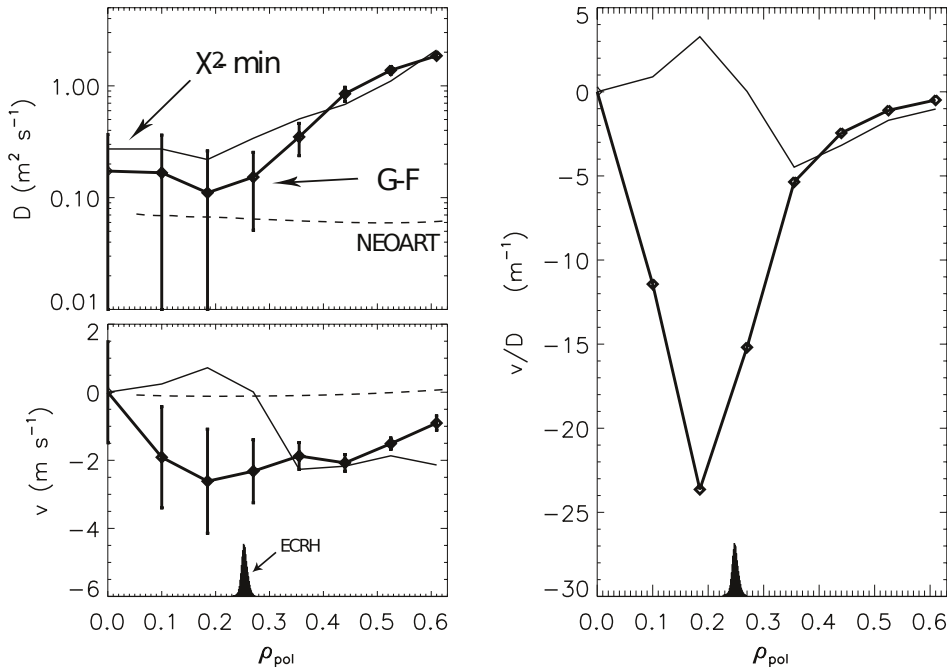

Figure 5. *Transport parameters for the quasi-stationary phase II (t < 3.075 s) of the Ar injection in discharge #25447.*

of the argon impurity injection for a large set of D and v starting with the values obtained through the G-F relation have been performed and the simulated LoS-integrated SXR emissivity fitted to the experimental data (assumed to have a 5% error). The quality of the fit is defined by the total χ^2 considering all LoS within the diagnostic sensitivity range. Since the LoS below and above the magnetic axis have
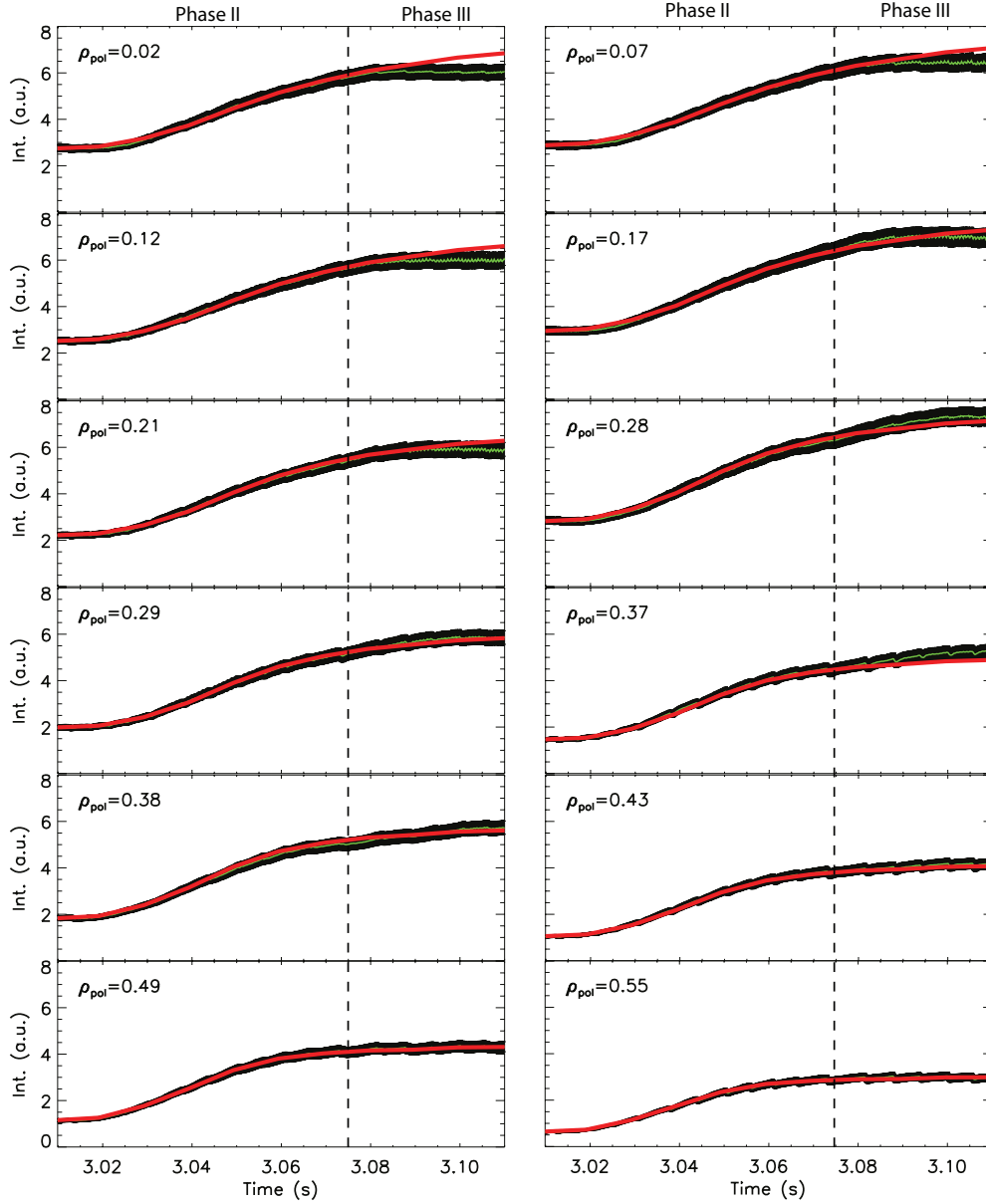

Figure 6. *Comparison of the experimental SXR LoS brightness and its simulation using the $\chi^2 - min$ transport parameters in figure 5 for the whole time-range up to the sawtooth crash (not show).*

different acquisition and amplification circuits, in order to avoid systematic errors due to hardware differences, this comparison has been limited to the top LoS. The pair of D and v profiles corresponding to the lowest total χ^2 is then used for the next scan. The final results (light continuous black lines in figure 5, labelled χ^2-*min*) are consistent with the G-F values for $\rho_{pol} > 0.35$ while, especially the convection coefficient, show substaintial differences inside this radius.

The dashed lines in 5a and 5b are theoretical estimates of neoclassical diffusion and convection coefficients evaluated using NEOART [29] assuming impurity concentrations of $5 \cdot 10^{-3}$ carbon, $5 \cdot 10^{-3}$ oxygen, $3 \cdot 10^{-5}$ tungsten, $1.5 \cdot 10^{-2}$ nitrogen and $3.5 \cdot 10^{-4}$ argon constant in time and along the radius. The nitrogen concentration has been deduced from a similar discharge (same heating, electron density and D_2 gas puff rate) while tungsten and argon concentrations have been evaluated through passive spectroscopy measurements (see [25] and [17] respectively). It is clear that both $\chi^2 - min$ diffusion and convection coefficients differ largely from the predicted neoclassical values along the whole radial range.

When comparing the STRAHL simulation using the $\chi^2 - min$ transport coefficients with the experimental LoS-integrated SXR emissivities (figure 6, simulation in red, data in green with black error bars) the agreement is very good for all lines of sight of camera H in the quasi-stationary phase II ($t < 3.075\ s$). Extending the comparison to the saturation phase III, the outermost LoSs (figure 6, $\rho_{pol} \geq 0.38$) are still well characterised, but the simulation drastically overestimates the peaking of the SXR brightness inside $\rho_{pol} \leq 0.21$. The change in transport is therefore occurring only within this radius which approximately coincides with the
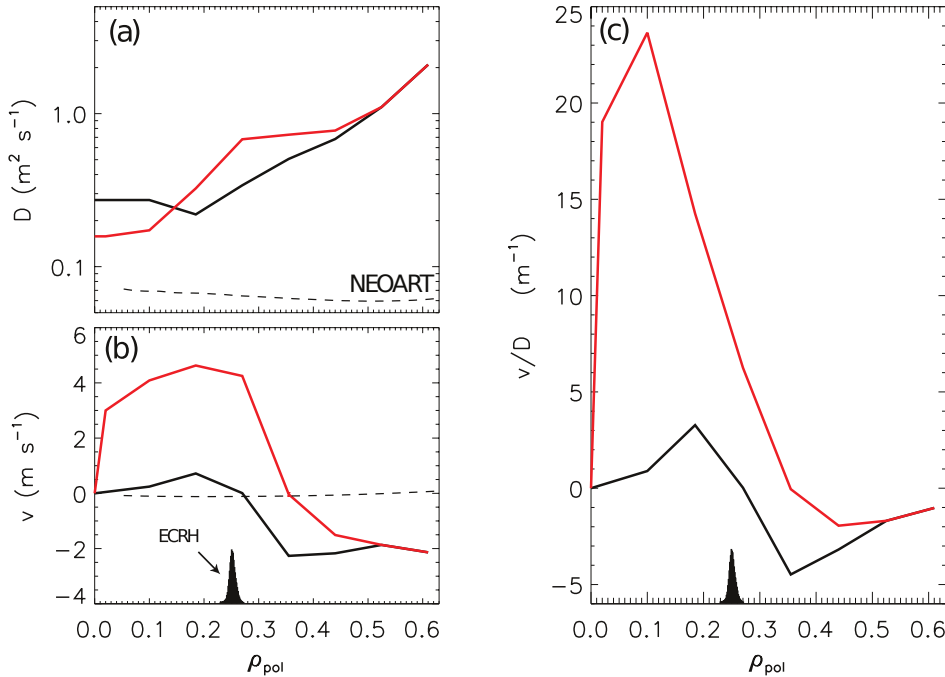

Figure 7. *Final transport parameters for the quasi-stationary phase II (t < 3.075 s, black) and the saturation phase III (3.075 < t < 3.11 s, red).*

position of the q=1 surface, i.e. only in the region of plasma where the $(1,1)$ mode is present.

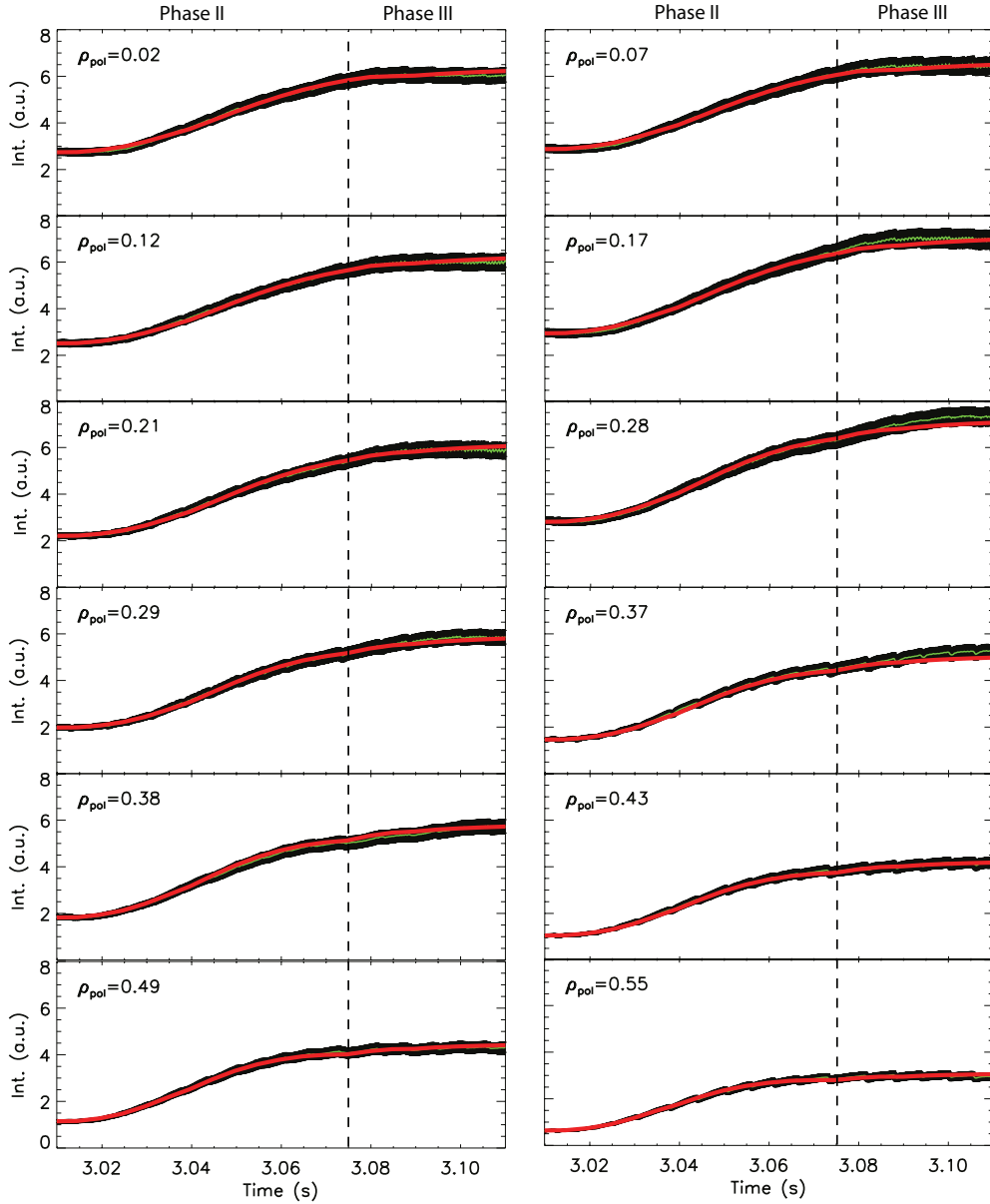

Figure 8. *Comparison of the experimental SXR LoS brightness and its simulation using the transport parameters in black in figure 7 up to (t < 3.075 s (quasi-stationary phase II) and those in red for t > 3.075 s (saturation phase III).*

4.2. Phase III: strong mode activity

The transport coefficients for phase *III* have been evaluated performing STRAHL simulations for the whole time-range $(3.015 - 3.11 \ s)$ using the first set of transport coefficients (figure 5) up to $3.075 \ s$ and searching for a second set that minimises the total χ^2 for the remaining range. The final results are shown in figure 7, the transport coefficients of phase *II* in black, the ones of phase *III* in red. The comparison of simulated versus experimental SXR brightness (figure 8) shows quite a good match for all LoS throughout the whole time range, although discrepancies are clearly visible for LoSs inside $\rho_{pol} \leq 0.37$.

When looking back to the background sawtooth cycles (figure 3), it is clear that the reason for this discrepancy is that the background SXR brightness in phase *III* cannot be considered constant anymore. While for phase *II* the estimated background changes are $< 10\%$ with respect to the intensity increase caused by the Ar, the variations in phase *III* are of the order of 30% and therefore influence substantially the time evolution of the argon signal. Since the background evolution in phase *III* is clearly non-linear and the onset and length of the different phases (*I* through *III*) change slightly from cycle to cycle (see figures 3 and 4), a subtraction of extrapolated background sawtooth cycles as performed e.g. in [19, 12, 17] is not possible. There is therefore no way of consistently estimating the argon transport coefficients for phase *III*. Since this is due to the strong W contribution to the background SXR signals (in comparison to the Ar signal caused by the injection), the background cycles themselves can be used to calculate the transport coefficients of W.

5. Evolution of the intrinsic W density

As already stated in 3.1, the signals of the SXR diagnostic in AUG are usually dominated by the emissions of intrinsic W. This is due to the fact that W is still not fully ionised in the plasma centre (Ga-like W^{43+} can be found at $T_e(0) \sim 3 \ keV$) so the emissions from line radiation are very strong in the SXR region. For electron temperatures $T_e > 3 \ keV$ for example, this translates in three orders of magnitude higher radiated power per ion with respect to a low-Z impurity such as boron ($n_W/n_e \sim 10^{-5}$ tungsten ions will radiate as much as $n_B/n_e \sim 0.01$).

The strength of W contribution to the SXR brightness depends therefore on the electron temperature (through the radiation loss parameter L_W^{sxr}) as well as on the concentration of W and of low-Z impurities. This has to be examined on a shot-to-shot basis, if not for different phases of the same discharge. To demonstrate the validity for the present case, the time-evolution of the intrinsic W density throughout the whole flat-top of discharge #25447 has been evaluated using equation 5 assuming tungsten as only radiator. If the SXR channels used for the analysis have a correct relative calibration and the shape of the SXR-filtered radiation loss parameter L_W^{sxr} is trustworthy, then the computed W-density profile will have the same shape as the *real* one, its absolute value to be rescaled through a multiplication constant. This constant can be estimated by comparing the result with calibrated passive tungsten spectroscopy measurements from the grazing incidence spectrometer (GIW). This diagnostic detects VUV light around $5 \ nm$ and the concentration is calculated for two groups of spectral features [25]:

(i) quasi-continuum ($c_{W,qc}$): envelope of compound emissions from ionization stages $W^{27+} \rightarrow W^{35+}$

(ii) spectral-lines ($c_{W,l}$): contributions from ionization stages $W^{41+} \rightarrow W^{45+}$

Since these contributions come from different ionization stage groups, their emission will come from different regions of the plasma, their position depending on the electron temperature and the ionization and recombination rates [25]. Summing over the fractional abundance profiles of all ionization stages participating in the measurement $f_{tot}(\rho) = \sum_q f_{W,q}(\rho) = \sum_q n_{W,q}(\rho)/n_W(\rho)$, the shape of the local emissivity profile can be calculated (equation 6) which can then be used to evaluate the average position of emissivity (equation 7) and the width of the emission shell (equation 8):

$$\epsilon_W(\rho,t) \propto n_e(\rho,t)^2 \ c_W(t) \ f_{tot}(\rho, T_e(t)) \tag{6}$$

$$\overline{\rho}(t) \quad = \int \rho \ \epsilon_W(\rho,t) \ dl \ / \int \epsilon_W(\rho,t) \ dl \tag{7}$$

$$\sigma_\rho(t) \quad = \sqrt{\int (\rho - \overline{\rho}(t))^2 \ \epsilon_W(\rho,t) \ dl \ / \int \epsilon_W(\rho,t) \ dl} \tag{8}$$

These equations are identical to those given in [17] for argon, but here the fractional abundance is that of the envelope of ionization stages taking part in the measurement and the local emissivity profile has been calculated ignoring the profile of the emissivity rate coefficient. The latter is admissible owing to the fact that the emission rate coefficients are nearly constant in the range of temperatures where the ionization shell is localised [25]. These rate coefficients are therefore applied as weighing factor to the fractional abundance shells. Finally, being the GIW measurements LoS-integrated, the evaluated c_W can be interpreted as the average over the radial range of emission weighed over the fractional abundance envelope f_{tot}.

The moment the emission shells taking part in the GIW concentration measurements are known, the SXR Abel-inverted W density profiles $n_W^{SXR}(r,t)$ can be integrated along the GIW LoS, weighed on the fractional abundance envelope and compared to the GIW values.

$$c_W^{SXR}(t) = \int n_W^{SXR}(\rho,t) \ f_{tot}(\rho,t) \ / \ n_e(\rho,t) \ dl \tag{9}$$

The ratio GIW/SXR for $c_{W,l}$ averaged over the whole time-range of interest then yields the multiplication factor for the rescaling of the SXR W density $\left\langle c_{W,l}(t)/c_{W,l}^{SXR}(t) \right\rangle$.

The post-rescaling comparison of the two measurements for both the spectral-lines (figure 9a, GIW in black SXR in red) and the quasi-continuum (figure 9b, GIW in black SXR in blue) shows that the tungsten density evaluated from the Abel-inverted SXR data is consistent with the passive spectroscopy measurement for most part of the discharge. Disagreement of the two measurements occurs only close to the Ar puffs (at 3.0 s and 4.8 s, as labelled in figure 9a) and in the beginning of the discharge ($t < 2.5 - 2.6 \ s$) where the electron temperature (figure 9c) is close to the detection limit of the spectral-lines.

Errors of 20% have been assumed on the GIW measurements (due to plausible inaccuracies in the atomic data), while the errors on the SXR-evaluated W concentration result from a full propagation of errors of the Abel-inversion, electron density and radiation loss parameter. Since the latter is non-linear in T_e, its value and error have been calculated using the upper and lower estimates of the electron temperature:

$$\langle L_A^{sxr} \rangle \ = \frac{L_A^{sxr}(T_e + \sigma_{T_e}) + L_A^{sxr}(T_e - \sigma_{T_e})}{2} \tag{10}$$
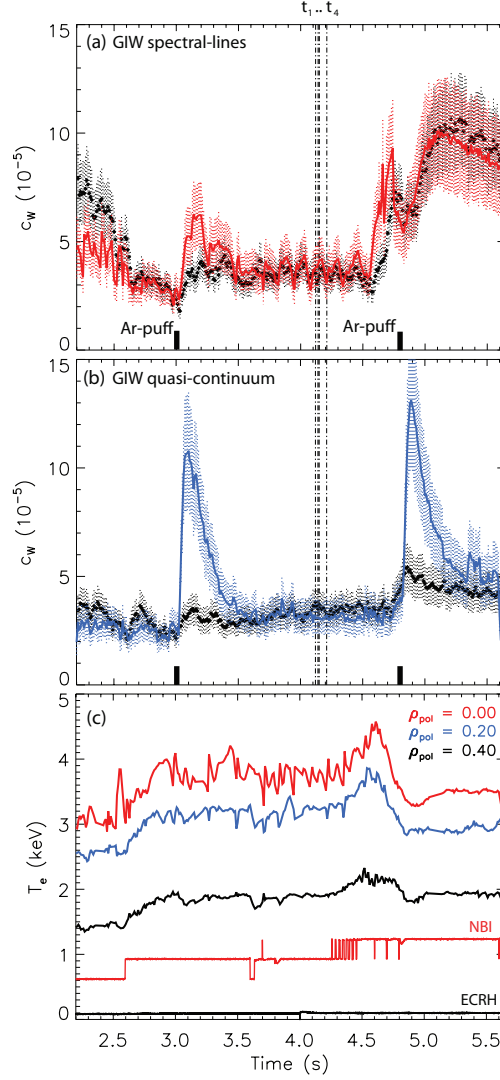
Figure 9. *Tungsten concentration measurements from passive spectroscopy (GIW, in black, (a) from spectral lines, (b) from the quasi-continuum as described in the text) compared to SXR-evaluated W concentration (red and blue in (a) and (b) respectively) throughout the flat-top of discharge #25447. Electron temperature at different radii, NBI injected heating power and ECRH power (c, as labelled).*

$$\sigma_{L_A^{sxr}} = \frac{|L_A^{sxr}(T_e + \sigma_{T_e}) - \langle L_A^{sxr} \rangle| + |\langle L_A^{sxr} \rangle - L_A^{sxr}(T_e - \sigma_{T_e})|}{2} \quad (11)$$

5.1. v/D profiles of the intrinsic W density

As demonstrated by the above results, in the time-range of the background cycles shown in figure 3 and 4, the SXR Abel-inverted intrinsic tungsten density measurement is consistent with independent passive spectroscopy measurements. The tungsten

transport coefficients could therefore in principle be evaluated using the G-F relation (equation 3). On the other hand, the signals in the quasi-stationary phase *II* show only moderate changes (i.e. small W fluxes) which would lead to large errors in the separate evaluation of D and v. In the saturation phase *III* the fluxes are strong but concurrent with changes in the electron temperature. Separate estimates of diffusion and convection cannot therefore be calculated reliably, but their ratio $v/D = \nabla n_W/n_W$ at the end of the quasi-stationary phase *II* and saturation phase *III*, can be estimated. This requires the assumption that the ion flux $\Gamma_W \approx 0$, approximation that holds inside the q=1 surface (stiff profiles) for time-points $t_1 \rightarrow t_3$ and for t_4 assuming the expulsion of W ions from inside the q=1 surface has reached equilibrium before the sawtooth crash.

The second background cycle in figure 4 has been chosen due to the availability of IDA measurements in the phases of interest. The electron density and temperature profiles (figures 10a and 10b respectively), the tungsten density and the v/D profiles (figures 10c and 10d respectively) are shown for four time-points along the sawtooth cycle (vertical dashed black lines in figures 4 and 9), labelled $t_1 \rightarrow t_4$. The first three time-points are all in the quasi-stationary phase *II* ($t_1 \rightarrow t_3$, low mode activity) and show a barely noticeable, stiff increase of the W density inside the q=1 surface. The forth one is at the end of the saturation phase *III* (t_4, mode saturation), just before
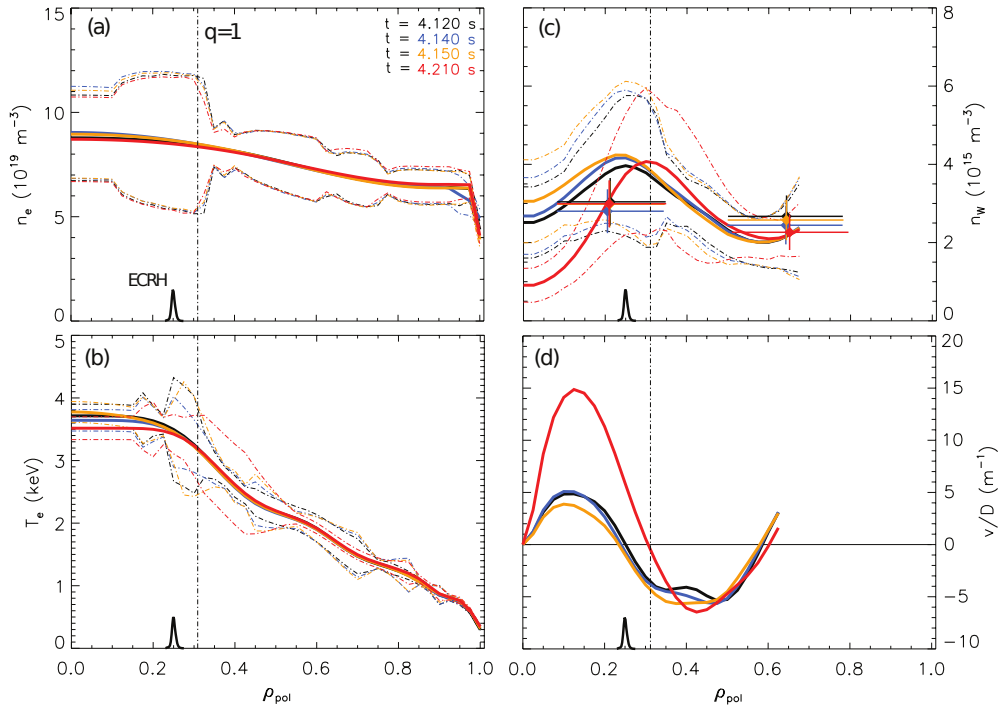

Figure 10. *Electron density (a) and temperature (b) profiles, tungsten density profiles (c) and v/D ratio (d) for the times labelled on the top right and shown as dashed black vertical lines in figures 4 and 9. Upper and lower limits of profiles defined by their error bars are shown as dashed-dot lines of the same colour. The position of ECRH deposition as evaluated by TORBEAM [30] and of the $q = 1$ surface are also shown.*

the sawtooth crash.

Both electron density and temperature profiles are relatively constant throughout the whole cycle, apart from a slight flattening inside the $q = 1$ surface. The tungsten density profile (figure 10d) is hollow in all four time-points considered, but the hollowness increases drastically during mode saturation (red in figure 10). The v/D profiles in the quasi-stationary phase *II* ($t_1 \rightarrow t_3$ in figure 10d) match very well both the shape and absolute values of those of Ar (figure 6), with a maximum at $\rho_{pol} \sim 0.1 - 0.2$ and a minima at $\rho_{pol} = 0.4$, showing only slight differences in the absolute values. For the saturation phase *III* (red in figure 10d), an increase in hollowness is seen with respect to the quasi-stationary phase *II*, but the maximum at $\rho_{pol} \sim 0.15$ is almost a factor two lower in absolute value with respect to those evaluated for argon. The values outside $\rho_{pol} > 0.5$ see almost no modification over the whole cycle.

The large error bars in the W density are mainly a consequence of the propagation of errors from the electron density profiles. In 2009 when the analysed discharge was performed, the most central LoS of the DCN interferometer (used for the IDA fits) didn't reach the plasma centre (see e.g. [31]). Recently, the $H3$ LoS has been modified and now goes through the plasma centre. The precision of the IDA fits will therefore be highly increased in the next campaigns and this will be reflected in the W density in future analyses.

6. Discussion and conclusions

The results presented in sections 4 and 5 undoubtedly demonstrate that the presence of long-lived $(m, n) = (1, 1)$ internal kink MHD activity in sawtoothing plasmas can lead to strong variations in impurity transport, despite the relatively constant mode-averaged main plasma parameters. The example discharge reported is a typical case for AUG when central ECRH heating is used. In these cases the sawtooth cycles are often characterised by saturated $(1, 1)$ modes lasting large fractions of the sawtooth period. The time evolution of both the electron temperature and SXR brightnesses depends heavily on the deposition position of the ECRH with respect to the $q = 1$ surface. For deposition close to the $q = 1$ surface as in the reported example, the cycles are typically very long ($\tau_{ST} \sim 100 \ ms$) and exhibit three phases which are clearly distinguishable in the electron temperature time-traces of the ECE diagnostic. Just after the sawtooth crash a short recovery phase lasting $0.1 \times \tau_{ST}$ is distinguished by a sharp increase of the electron temperature inside the $q = 1$ surface and by a more pronounced peaking of the SXR signals. A quasi-stationary phase lasting $0.5 \times \tau_{ST}$ follows, with low mode activity and only slight changes in mode-averaged plasma parameters. This is then followed by the fast growth of a $(m, n) = (1, 1)$ which saturates and survives typically $0.4 \times \tau_{ST}$ before the next sawtooth crash occurs. During this last phase, the SXR profiles are seen to become increasingly hollow.

Differently from those cases where no saturated modes are present, the time evolution of the SXR background in these cycles is clearly non-linear and the onset and length of the different phases change slightly from cycle to cycle. The background SXR evolution during a sawtooth cycle cannot therefore be extrapolated for cycles of different durations and a subtraction of background sawtooth cycles as performed e.g. in [19, 12, 17] is not possible. These background effects and the changes in transport occurring during the sawtooth cycle lead therefore to unrecoverable errors in the evaluation of transport parameters through trace impurity injection.

The alternative solution for the analysis of impurity transport proposed in this contribution relies on the analysis of the background SXR signals only and is applicable to those cases in which the intrinsic W dominates the SXR emission (as is the case for AUG and JET since the installation of the ITER-like wall [32]). The W density can then be calculated performing an Abel-inversion of the SXR signals, calculating the W density assuming W as only radiator and applying a rescaling factor evaluated from passive spectroscopic measurements. Comparison the time evolution of the result with that of passive spectroscopy measurements gives a very good match within the experimental uncertainties. Applying this method to the sawtooth cycles described above reveals that the hollowness of the SXR emissivity profiles corresponds to a hollowness in the W density and that, during mode saturation, W is expelled from the plasma centre and redistributed close or outside of the $q = 1$ surface. The uncertainties in the electron density profiles are still too large for a more precise assessment of the processes in action, but recent upgrades to the interferometer diagnostic at AUG should increase their precision for future application of the method.

The analysis presented averages however over mode rotation and does not account for the non-axisymmetric geometry due to the presence of the saturated $(1, 1)$ mode, so can give only a qualitative description of the processes in action. A fully two-dimensional analysis is thus required. If the number of SXR LoS and viewing angles is sufficient, tomographic techniques can be applied to the SXR data. A 2D mode-resolved map of the electron temperature can be computed relying on harmonic decomposition performed through short time Fourier transforms of the electron temperature measurements from the 1D ECE diagnostic [33]. For the electron density, the method for rotation tomography developed in [34] has been recently applied to fast-sweeping X-mode reflectometry data [35] delivering mode-resolved 2D maps of the electron density. Using these three techniques simultaneously, all quantities in equation 5 can be resolved in 2D, enabling the evaluation of the time-evolution of two-dimensional mode-resolved intrinsic W density. This can then shed light on the *real* (not mode-averaged) transport characteristics of W in the presence saturated $(1, 1)$ modes which is necessary to understand the interplay between central ECRH and MHD activity in mitigating central W accumulation. Since the explanation and application of the method requires space for in-depth discussions, details will be reported in a future publication.

Acknowledgments

References

[1] Fussmann G *et al* 1991 *Plasma Phys. Controlled Fusion* **33** 1677
[2] Angioni C *et al* 2006 *Physical Review Letters* **96** 095003–1
[3] McDermott R M *et al* 2011 *Plasma Physics and Controlled Fusion* **53** 124013
[4] Peeters A *et al* 2009 *Computer Physics Communications* **180** 2650 − 2672
[5] Casson F J *et al* 2010 *Physics of Plasmas* **17** 102305
[6] Belli E A *et al* 2008 *Plasma Physics and Controlled Fusion* **50** 095010
[7] Belli E A *et al* 2012 *Plasma Physics and Controlled Fusion* **54** 015015

[8] Angioni C *et al* 2014 *Nuclear Fusion* **54** 083028
[9] Casson F J *et al* 2015 *Plasma Physics and Controlled Fusion* **57** 014031
[10] Giroud C *et al* 2007 *Nuclear Fusion* **47** 313
[11] Parisot T *et al* 2008 *Plasma Physics and Controlled Fusion* **50** 055010
[12] Guirlet R *et al* 2010 *Nuclear Fusion* **50** 095009
[13] Menmuir S *et al* 2010 *Plasma Physics and Controlled Fusion* **52** 095001
[14] Delgado-Aparicio L *et al* 2011 *Nuclear Fusion* **51** 083047
[15] Valisa M *et al* 2011 *Nuclear Fusion* **51** 033002
[16] Howard N *et al* 2012 *Nuclear Fusion* **52** 063002
[17] Sertoli M *et al* 2011 *Plasma Physics and Controlled Fusion* **53** 035024
[18] Günter S *et al* 1999 *Nuclear Fusion* **39** 1535–1539
[19] Dux R *et al* 1999 *Nuclear Fusion* **39** 1509–1522
[20] Nave M F F *et al* 2003 *Nuclear Fusion* **43** 1204–1213
[21] Pütterich T *et al* 2013 *Plasma Physics and Controlled Fusion* **55** 124036
[22] Dux R STRAHL User Manual Laborbericht 10/30, IPP Garching, September 2006
[23] Igochine V Hotlink bases Soft X-ray Diagnostic on ASDEX Upgrade Technical Report 1/338, IPP, Garching, Germany, May 2010
[24] Kallenbach A *et al* 2005 *Journal of Nuclear Materials* **337-339** 732–736
[25] Pütterich T *et al* 2008 *Plasma Physics and Controlled Fusion* **50** 085016
[26] Rathgeber S K *et al* 2010 *Plasma Physics and Controlled Fusion* **52** 095008
[27] Fischer R *et al* 2008 *Plasma Physics and Controlled Fusion* **50** 085009
[28] Fischer R *et al* Multiple Diagnostic Data Analysis of Density and Temperature Profiles in ASDEX Upgrade in *Europhysics Conference Abstracts (CD-ROM, Proc. of the 36th EPS Conference on Plasma Physics, Sofia, 2009)*, edited by Mateev M *et al*, volume 33E, pages P–1.159, Geneva, 2009, EPS
[29] Peeters A G 2000 *Physics of Plasmas* **7** 268–275
[30] Poli E *et al* 2001 *Computer Phys. Comm.* **136** 90–104
[31] Mlynek A *et al* 2011 *Nuclear Fusion* **51** 043002
[32] Matthews G 2013 *Journal of Nuclear Materials* **438, Supplement** S2 – S10
[33] Sertoli M *et al* 2013 *Nuclear Fusion* **53** 053015
[34] Nagayama Y *et al* 1990 *Review of Scientific Instruments* **61** 3265–3267
[35] Nicolas T *et al* 2012 *Physics of Plasmas* **19** 112305